Neuron
Article

Inducing Gamma Oscillations and Precise Spike Synchrony by Operant Conditioning via Brain-Machine Interface

Ben Engelhard,[1,3,*] Nofar Ozeri,[1] Zvi Israel,[2] Hagai Bergman,[1,3] and Eilon Vaadia[1,3]
[1]Department of Medical Neurobiology, Institute of Medical Research Israel-Canada, The Hebrew University-Hadassah Medical School
[2]Center for Function and Restorative Neurosurgery, Department of Neurosurgery
Hadassah University Hospital, Jerusalem 91120, Israel
[3]Edmond and Lily Safra Center for Brain Sciences, The Interdisciplinary Center for Neural Computation, The Hebrew University, Jerusalem 91904, Israel
*Correspondence: ben.engelhard@mail.huji.ac.il
http://dx.doi.org/10.1016/j.neuron.2012.11.015

SUMMARY

Neural oscillations in the low-gamma range (30–50 Hz) have been implicated in neuronal synchrony, computation, behavior, and cognition. Abnormal low-gamma activity, hypothesized to reflect impaired synchronization, has been evidenced in several brain disorders. Thus, understanding the relations between gamma oscillations, neuronal synchrony and behavior is a major research challenge. We used a brain-machine interface (BMI) to train monkeys to specifically increase low-gamma power in selected sites of motor cortex to move a cursor and obtain a reward. The monkeys learned to robustly generate oscillatory gamma waves, which were accompanied by a dramatic increase of spiking synchrony of highly precise spatiotemporal patterns. The findings link volitional control of LFP oscillations, neuronal synchrony, and the behavioral outcome. Subjects' ability to directly modulate specific patterns of neuronal synchrony provides a powerful approach for understanding neuronal processing in relation to behavior and for the use of BMIs in a clinical setting.

INTRODUCTION

Neural oscillations are an important computational mechanism that reflect coordinated activity in the brain (Buzsáki and Draguhn, 2004; Fries, 2009). In particular, oscillations in the low-gamma frequency (around 30–50 Hz) have been observed in a variety of tasks, conditions, and brain areas (Herrmann et al., 2010). In several studies, spike activity has been found to be phase locked with oscillations in the local field potential (LFP) (Gray and Singer, 1989; Murthy and Fetz, 1996), supporting the view that low-gamma oscillations are involved in synchronization of neuronal groups in a functionally relevant manner (Gray et al., 1989), potentially functioning as a mechanism for integrative binding (Singer, 1999). Additionally, precise synchrony has been suggested to mediate neural coding and in several studies has been linked to behavior (Shmiel et al., 2005; Riehle et al., 1997; Kayser et al., 2009). However, the relationship between neuronal oscillations as detected by LFP or EEG, single-unit spike synchrony, and behavior is still the subject of intensive research and debate (Palanca and DeAngelis, 2005; Shadlen and Movshon, 1999; Nunez and Srinivasan, 2010).

One particular line of research has linked measures of synchrony as detected by network oscillations with pathological brain states. Abnormal measures of low-gamma EEG have been detected in autism, ADHD, Alzheimer's disease, schizophrenia, and other medical conditions (Uhlhaas and Singer, 2006). It has been hypothesized that such abnormalities may reflect impairment in neural synchrony that can cause cognitive deficits. For example, patients with schizophrenia show reduced evoked oscillations in the gamma range following auditory and visual stimulation and also present reduced nonstimulus-locked oscillations during the processing of visual stimuli (Uhlhaas and Singer, 2010; Herrmann and Demiralp, 2005). Children and adolescents with autism have been reported to exhibit significantly reduced left-hemispheric 40 Hz EEG oscillations following the presentation of monaural click trains (Wilson et al., 2007). Patients with Alzheimer's disease present decreased low-gamma EEG synchronization in the resting state (Koenig et al., 2005). These results suggest that modulation of neural synchrony in a controlled manner by way of gamma oscillations could ameliorate some of the deficits caused by various pathological conditions and advance our understanding of the relationship between these neurophysiological parameters and behavior.

Fetz pioneered the use of the brain-machine interface (BMI) to modulate the firing rates of single neurons in an operant-conditioning paradigm (Fetz, 1969). Here, we used a similar paradigm to specifically increase the power of a 30–43 Hz band of LFP (termed "low-γ" in this article) in selected sites of the motor cortex using a 96-electrode array. Monkeys learned to generate gamma oscillations and use the BMI to move a cursor on the screen and obtain a reward. As the low-γ power increased, we observed phase locking of spikes to the low-γ oscillations and increasingly precise spike synchrony. Finally, direct neural control of LFP oscillations in a specific locality in cortex led to a corresponding spatial pattern of spike synchrony.

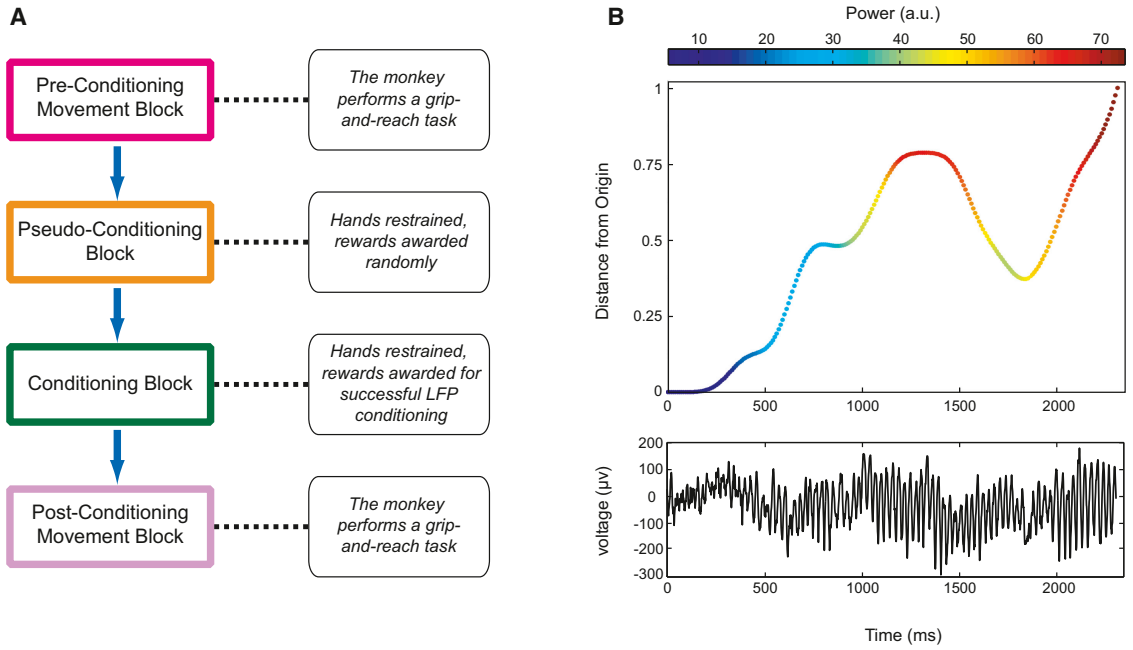

Figure 1. Task Design

(A) Experimental block design of a single session.

(B) Single-trial example of the relationship between cursor position and LFP power of the 30–43 Hz band during the conditioning block. Top view shows cursor distance from origin as a function of time (0 is origin, 1 is target location). The 30–43 Hz power is color coded. Bottom view shows the LFP trace from a single conditioned site during this trial. a.u., arbitrary units.

RESULTS

Conditioning the Power of the Low-γ Band

We recorded LFPs and single-unit activity using a 96-microelectrode array implanted in the arm region of the primary motor cortex. To teach the monkeys to generate low-γ oscillations in a controlled manner, the daily recording session was divided into four blocks (Figure 1A). The main part of the session was the conditioning block (the third block) where the monkeys' arms were comfortably restrained, and a cursor on the screen moved from the center (origin) toward one of eight targets, chosen randomly once for the entire block. The position of the cursor at time *t* was correlated with the mean power of the low-γ band of LFP recorded from a chosen group of four electrodes in a window of 500 ms preceding *t*. When the cursor moved from the origin and reached the target, a liquid reward was delivered. LFP power was evaluated every 100 ms, and an interpolation method was used to provide the appearance of smooth cursor movement (Figure 1B, top; see Experimental Procedures).

The other three blocks were used as controls. The second block was termed the pseudoconditioning block and presented the same conditions as the conditioning block except that the cursor position was chosen randomly every 100 ms, and hence, rewards were delivered randomly as well; in this block as well, the interpolation method provided the appearance of smooth cursor movement. The first and last blocks (movement blocks) consisted of a center-out grip-and-reach task on which the monkeys had previously been trained. These two blocks were used to allow comparison of neuronal activity during conditioning to activity in natural behavior. The last block served as a control for the recording stability of single units in the session.

Behavioral Performance

In the first sessions, the monkeys did not manage to significantly increase the low-γ power; their performance improved gradually until a clear ability to increase power was evidenced. Figures 2A and 2B show the low-γ power of LFP recorded from a single electrode used for conditioning (hereafter referred to as a "conditioned site") during the entire 1st and 23rd sessions of monkey M. The monkey learned in the latter sessions to reliably increase the power in the conditioning block. Note that the power also increased somewhat in the pseudoconditioning block but remained distinctly lower. The generation of some low-gamma oscillations in this block could reflect imperfect extinction of the conditioning acquired in previous sessions because the random reward schedule in the block did not explicitly prohibit gamma generation. To quantify the learning procedure, we calculated the mean low-γ power recorded from the conditioned sites during the whole conditioning block for each day and normalized it by the mean power recorded during the first movement block. The normalization removed some of the noise caused by day-to-day fluctuations in the total amount of power but did not affect the overall result (see Figure S1 available online). Plotting the normalized overall low-γ power for all sessions of monkey M (Figure 2C) showed consistent improvement in the control capacity (linear fit: $\rho = 0.86$).

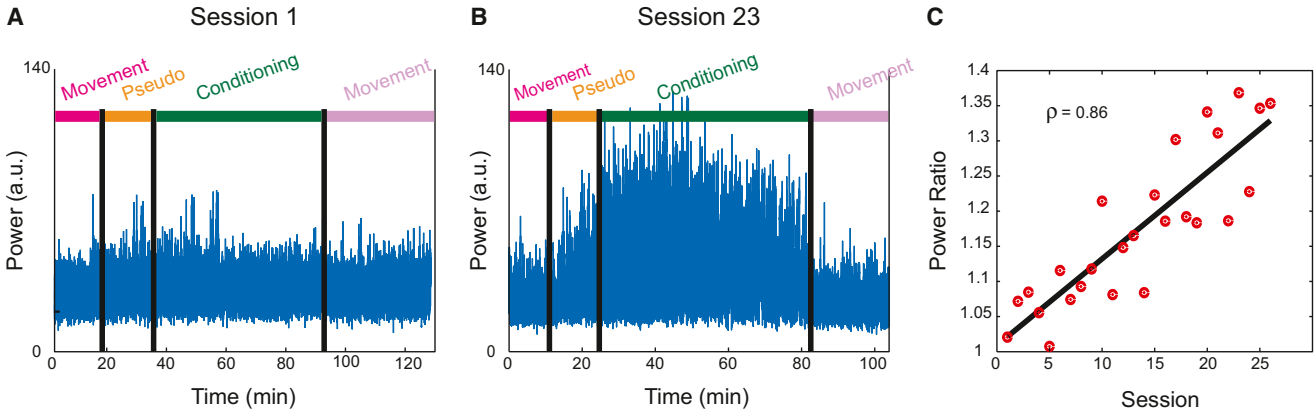

Figure 2. Improvement of Performance across Conditioning Sessions

(A) Power of the 30–43 Hz band during the complete first session of monkey M.

(B) Power of the 30–43 Hz band during the 23rd session of monkey M.

(C) Ratio of average power in the conditioning and preconditioning movement blocks across sessions for monkey M.

See also Figure S1.

Induced Narrow-Band Activity

As a first step in the analysis of the induced LFP during conditioning, we tested whether the increase in power was specific to the selected band. In particular, we examined the signal to avoid general broadband effects that could reflect various artifacts (Yuval-Greenberg et al., 2008). Figure 3 shows the induced low-γ oscillations in monkeys M and Q. Figure 3A shows the LFP during a control trial in the pseudoconditioning block (monkey M), with no signs of low-γ activity, whereas Figures 3B and 3C (monkeys M and Q, respectively) are single trials in the conditioning block showing strong low-γ activity preceding the reward.

The power spectra of the 500 ms preceding reward are shown in the bottom panels in Figures 3A–3C. As expected, during the control trial, the LFP power decline was approximately proportional to 1/f (Figure 3A, bottom). In contrast, during the conditioning block, we observed a very narrow peak around 34 Hz (Figures 3B and 3C, bottom). The peak widths at half-height were 2.9 and 3.2 Hz. The effective increase was thus in an even narrower band than the one required by the algorithm.

Once the monkeys learned the task, the capacity to evoke high-amplitude narrow-band LFP activity was robust. Figure 4A depicts ten consecutive traces of LFP preceding reward in the conditioning block of one of the latter sessions. The single traces all present clearly observable oscillations in the low-γ range. To examine the mean LFP activity preceding reward, we averaged time windows locked to the first peak of the gamma cycle (phase = 0) around 500 ms before reward onset (see Experimental Procedures). The mean LFP activity is plotted in Figure 4B for the first movement block (magenta), the pseudoconditioning block (yellow), and the conditioning block (green). We observed a clear increase in amplitude in the conditioning block alone. Additionally, we plotted the mean spectra for these blocks (Figure 4C), which validated this result; a robust peak at 35 Hz (with a width at half-height of 7.2 Hz) was only observed in the conditioning block. Similar results were obtained for all successful conditioning sessions (Figure S2). Thus, although there were fluctuations between spectra of single trials, the evoked activity was within a narrow band of the specified frequency.

Phase Locking of Spikes to the LFP

Single neurons can become synchronized if their responses are phase locked to commonly oscillating signals (Apostol and Creutzfeldt, 1974; Eckhorn et al., 1988; Gray and Singer, 1989; Tiesinga et al., 2008); this synchronization may have computational and behavioral consequences (Singer and Gray, 1995; Salinas and Sejnowski, 2001; Averbeck et al., 2006). We examined whether such spiking synchronization was elicited in our task. To do so, we first computed phase locking of single units to the LFP oscillations. Figure 5A shows the peri-event time histograms (PETHs) of two cells (magenta and green) and the mean LFP (black) in the conditioning block for a single recording session. The PETHs and LFPs were averaged using the first peak of the gamma cycle (phase = 0) around 500 ms before reward onset (see Experimental Procedures). The PETHs were computed using 1 ms bins and smoothed using a zero-phase Gaussian filter with SD of 2 ms. The PETHs of the two cells in Figure 5A exhibit clear amplitude locking and phase locking to the mean LFP in the 500 ms window preceding the mean reward delivery time. Both cells tended to fire in the falling flank of the LFP, as has been shown previously (Gray and Singer, 1989; Murthy and Fetz, 1996; Denker et al., 2011; see also Figure 6A). The average interval between the PETH peaks (Figure 5A, bottom) was 2.9 ms, well within the accurate timing required for a facilitatory effect on putative common target neurons (Abeles, 1991). To assess this phenomenon across the population, we computed the mean PETH for all units in all successful conditioning sessions (see Experimental Procedures). This analysis revealed phase locking in the population response for monkey M (Figure 5B) and monkey Q (Figure 5C). Oscillations in the LFP and phase-locked firing both disappeared rapidly after reward delivery.

Next, we quantified phase locking of spiking activity to the LFP and the relation between phase-locking strength and the low-γ

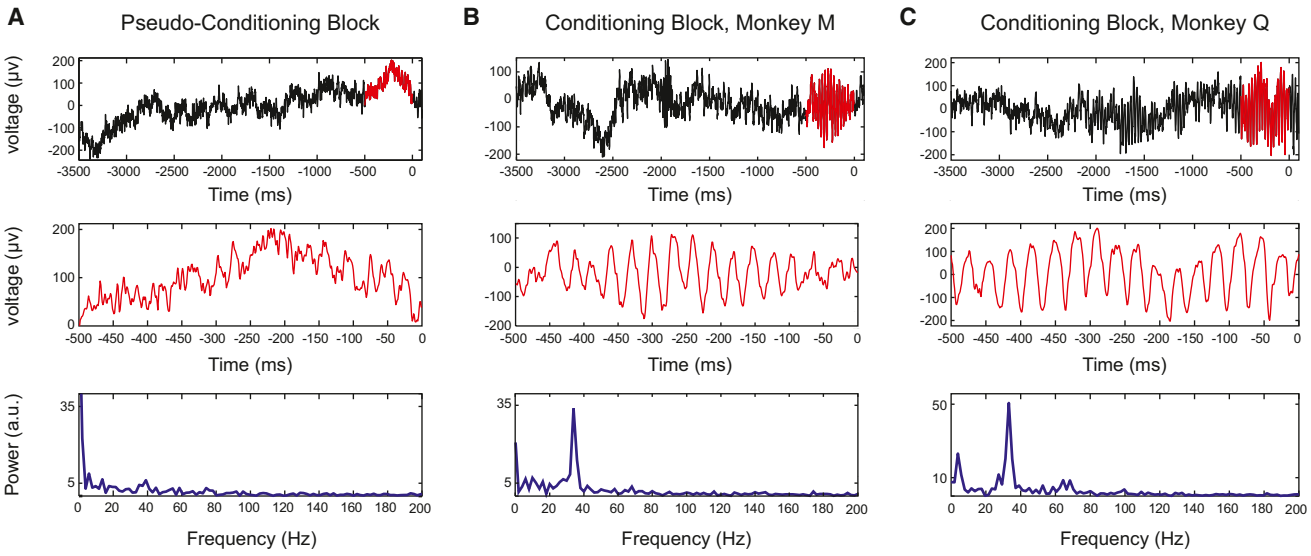

Figure 3. Single-Trial Examples Aligned to Reward Delivery

(A) Top view shows a raw LFP trace in the pseudoconditioning block. The 500 ms period before reward is highlighted in red. Middle panel is an expanded view of the 500 ms period before reward. Bottom view is a power spectrum of the 500 ms period before reward. Data for monkey M (session #20), similar traces were obtained for monkey Q (not shown).

(B) The same as in (A), but for a trial in the conditioning block, monkey M.

(C) The same as in (A), but for a trial in the conditioning block, monkey Q (session #17).

power. We tested the low-γ power in segments of 500 ms throughout the conditioning block. The 500 segments with highest power comprised the "High-Power period," and the 500 segments with lowest power comprised the "Low-Power period." Using the Hilbert transform (see Experimental Procedures), we constructed phase histograms of spike firing for all single units in the two periods.

Figures 5D and 5E depict these histograms for the two cells of Figure 5A. In the Low-Power period, both cells had uniform phase histograms (Raleigh test, $p > 0.28$). In the High-Power period, however, both cells exhibited highly significant phase locking (Figures 5D and 5E, right; Raleigh test, $p < 10^{-32}$). The time difference between their preferred firing times assuming a 35 Hz cycle was 2.82 ms, corresponding well with the PETH calculations.

For the population analysis, we calculated the significance of phase locking (Raleigh test with $p < 0.0001$, Bonferroni corrected) and the preferred phase for all single units ($n = 218$) in both the Low- and High-Power periods (Figure 5F). The results are striking and show that none of the units had significant phase locking in the Low-Power period, compared to 63.6% in the High-Power period.

Most units had their preferred phase in the falling flank of the LFP (0 to π). This constrains the differences between times of preferred firing within the gamma cycle and allowed us to quantify the proportion of units with preferred firing in a given time interval (Figure 5G); 50% of units with a significant preferred phase preferentially fired within 4 ms of each other, and for increasing proportions of units, the window of firing was still relatively short (e.g., 80% of units preferentially fired in an 8 ms window).

Thus, the gamma power as elicited in our task was accompanied by robust phase locking that can account for synchronization in short enough time windows to have a physiologically relevant integrative effect on target neuronal populations.

Visualizing and Quantifying Single-Unit Synchrony

To examine synchrony at the single-trial level, we present eight LFP traces from successful trials in a single recording session with spikes from all single units superimposed on the LFP (Figure 6A). Even at the single-trial level, the tendency of cells to fire in the falling flank of the LFP is clearly evident, resulting in multineuron temporal clustering. The temporal pattern of synchrony is demonstrated in a raster plot of the first 80 successful conditioning trials from the same day (Figure 6B).

We quantified the synchrony between several single units by computing the probability of coordinated firing of the units in a time window of 5 ms, normalized by the total number of spikes. In order to assess the relationship between low-γ power and synchrony, we divided the conditioning block into five periods of increasing low-γ power (see Experimental Procedures). We calculated the probability that a given number (n) of units fired in synchrony within a 5 ms window. For $n = 1$, this is the probability that only 1 unit fires in a 5 ms window. When the low-γ power was lower, the probability of nonsynchronous firing ($n = 1$) was higher (Figure 6C, $n = 1$). For 2 units ($n = 2$), this relationship was reversed; namely, units fired in pairs with a higher probability as the low-γ power increased (Figure 6C, $n = 2$). The same relationship held for groups of up to 6 units (we rarely saw more than 6 units firing together, which may well be a consequence of the limited number of simultaneously recorded units in our experiment). We thus found a clear relationship between low-γ power and spike synchrony: the higher the power, the higher the probability of coordinated firing of different units.

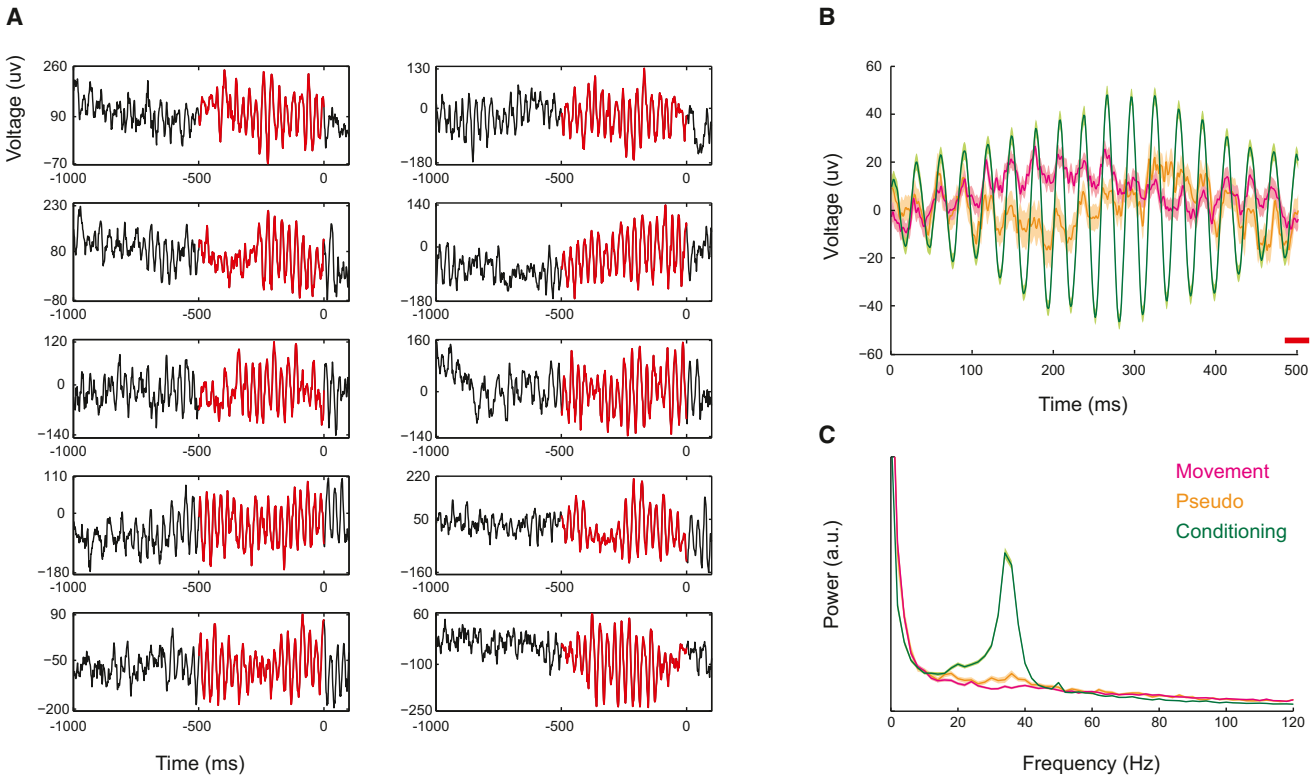

Figure 4. Single Trials and Trial Averages Showing Low-γ Oscillations in the LFP during Conditioning

The traces are shown for one conditioned site in one session.

(A) LFP traces aligned to reward delivery (time 0) in ten consecutive trials during the conditioning period. The 500 ms period before reward is highlighted in red.

(B) Average LFP traces preceding reward in the preconditioning movement (magenta), pseudoconditioning (yellow), and conditioning (green) blocks. SEM is in light shading (see Experimental Procedures for the averaging procedure). Time 0 is the first peak of the gamma cycle (phase = 0) around 500 ms before reward onset. The red horizontal bar indicates range of times of reward delivery.

(C) Average and SEM of power spectra of LFP traces preceding reward for the three blocks.

See also Figure S2.

Effect of Phase-Locked Firing on Pairwise Neuronal Correlations

The next step in the quantification of neuronal synchrony and its relation to phase locking involved a detailed study of the dynamics of pairwise neuronal correlations.

An example of temporal cross-correlation between 2 units during periods of Low Power and High Power is shown by the cross-correlation histograms (CCHs) in Figure 7A. Both units had strong phase locking during the High-Power period, as shown in Figures 5D and 5E. A highly significant central peak (shuffling test, $p < 10^{-6}$) appeared in the CCH for the High-Power period (Figure 7A, red). Additionally, the CCH was characterized by an oscillatory pattern at the low-γ frequency (the mean frequency of peaks in the −150 ms to +150 ms interval was 33.2 Hz). Note that the CCH reflects precise temporal synchronization in the range of a few milliseconds. In contrast, the blue trace in Figure 7A shows the CCH during the Low-Power period, with practically no temporal correlations between these 2 units (Figure 7G shows eight other pairs with similar CCH characteristics). The dynamics of pairwise correlations in relation to the temporal evolvement of low-γ oscillations were studied using joint peri-event time histograms (JPETHs) that were calculated for the High-Power period; with time zero (0) denoting the start of an aligned 500 ms segment in this period (see "Alignment of Neural Data" in the Experimental Procedures). An example is presented in Figure 7B, showing the JPETH for the same pair of cells whose CCH is shown in Figure 7A. Note the fine structure of peaks and troughs that reflect phase-locked firing of the 2 units. The temporal correlation between the units increased when the waves of phase-locked firing converged at the High-Power segment.

To visualize the similarity between the temporal structures of the spike synchrony of these 2 units and the instantaneous low-γ power recorded from their corresponding electrodes, we also computed the joint peri-event time average (JPETA) of the low-γ power of these electrodes (Figure 7D). The similar dynamics further illustrates the tight association between low-γ oscillations and temporal synchrony.

A more fine-grained view of the dynamics of the probability of joint firing along the trial is afforded by the main diagonal of the JPETH of Figure 7B shown in Figure 7C (black). This probability is modulated together with the low-γ power (Figure 7C, blue), illustrating the dynamic engendering of neural synchrony. Note

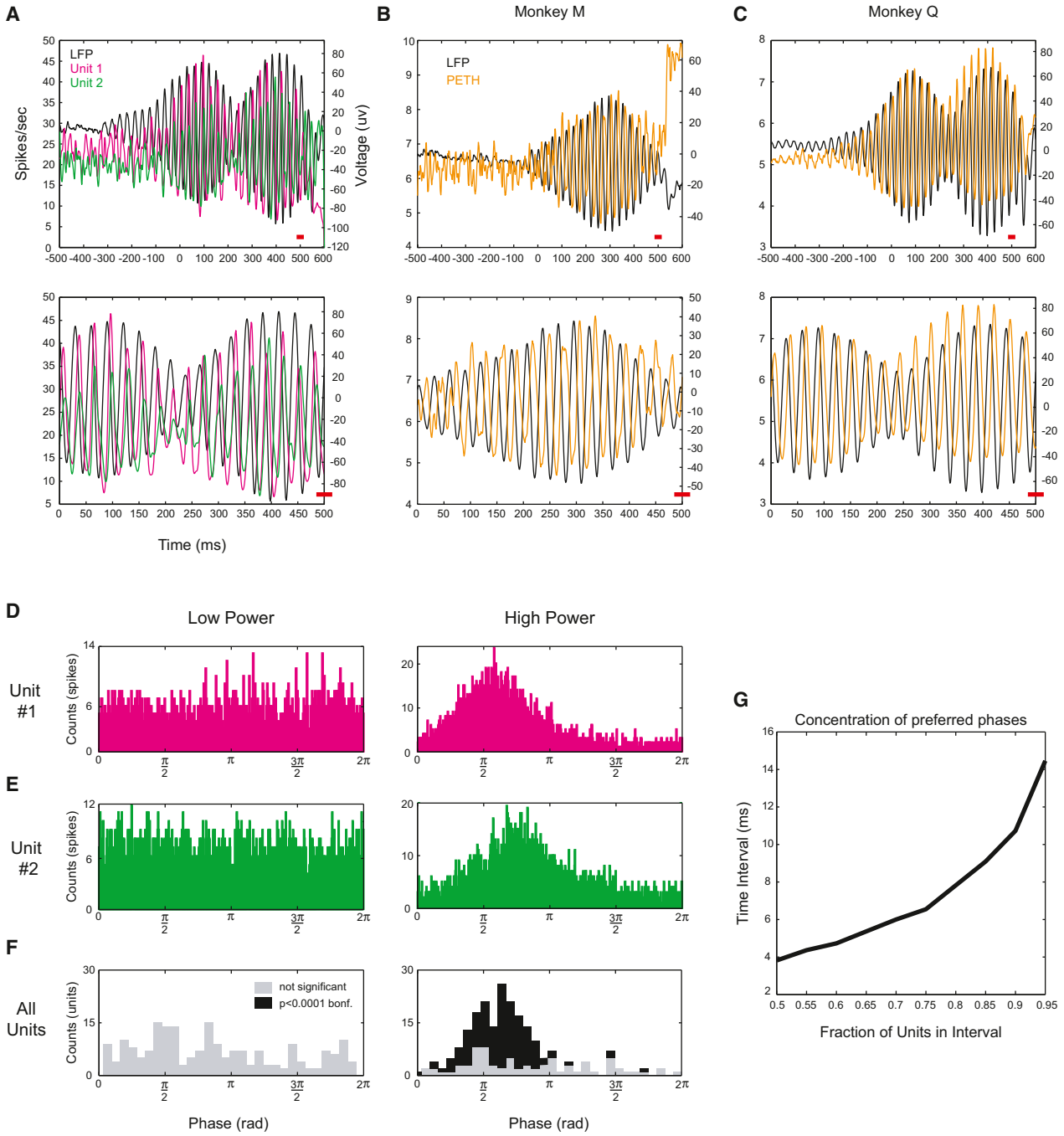

Figure 5. Phase Locking of Single Units to the Low-γ Oscillations

(A) PETH of 2 units (magenta and green) recorded simultaneously, and average LFP (black) in microvolts (y axis units on the right side of the plot). Time 0 is the first peak of the gamma cycle (phase = 0) around 500 ms before reward onset. The red horizontal bar indicates range of times of reward delivery. Bottom panel is an expanded view of the 500 ms period before reward.

(B) Population PETH and average LFP for successful sessions aligned to reward, monkey M, with expanded view in the bottom plot.

(C) Same as (B), for monkey Q.

(D) Histograms of low-γ phase at spike firing times for Unit #1 in (A) in the Low-Power (left) and High-Power (right) periods.

(E) Same as (D), for Unit #2 in (A).

(F) Histograms of preferred phases for all units for the Low-Power (left) and High-Power (right) periods. Counts of significant preferred phases are marked in black. bonf, Bonferroni corrected; rad, radians.

(G) Proportion of units (x axis) with a given preferred firing time interval (y axis). Note that 80% of the cells preferentially fired within 8 ms of each other. Proportion was computed for units with a significant preferred phase (see Experimental Procedures).

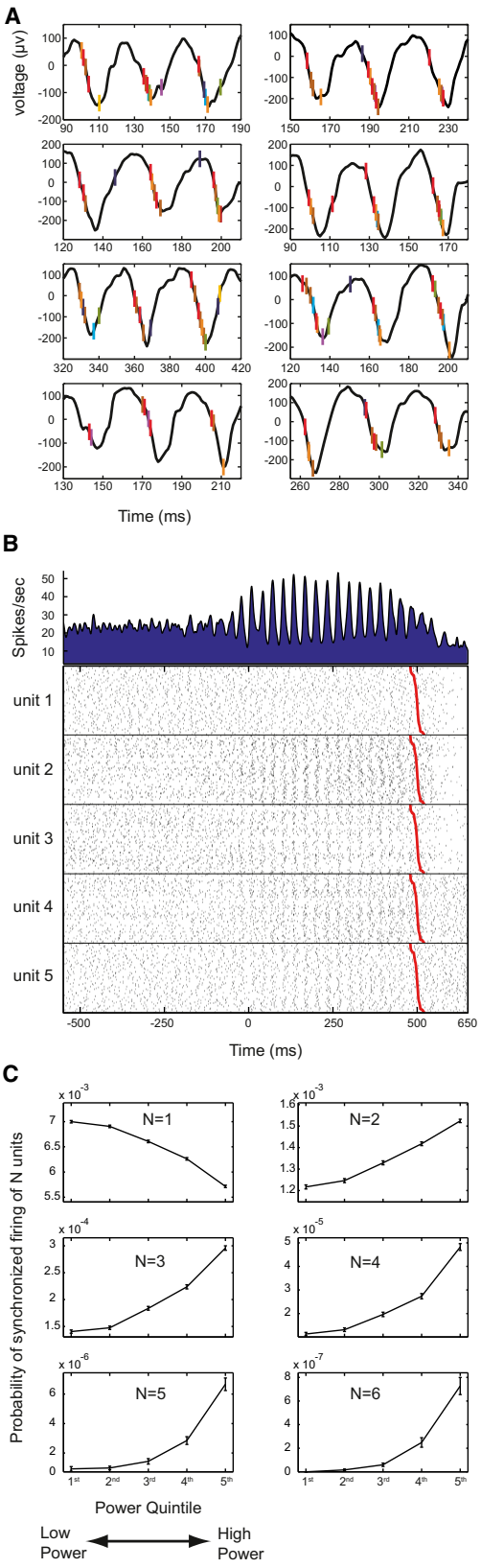

Figure 6. Temporal Synchronization of Single Units

(A) LFP traces (black) preceding reward (time = 500 ms) from one conditioned site over eight trials in the conditioning period with spikes from simultaneously recorded single units superimposed (colored). Spikes tended to cluster and occurred mostly in the falling flank of LFP.

(B) Raster plot and population PETH (top) for 5 units recorded simultaneously for the first 80 successful trials in the conditioning block. The trials in the raster are locked to the first peak of the gamma cycle (phase = 0) around 500 ms before reward onset. The red lines show times of reward delivery. Notice the temporal clustering during the 500 ms preceding reward, resulting in a phase-locked PETH (top).

(C) Probability of n recorded units to fire together in a 5 ms bin with n shown in each frame, for n = 1 to n = 6. This probability was calculated separately for five groups of periods of increasing power of low γ, shown on the x axis. Error bars are SEM.

that the spiking synchrony is also modulated at a finer timescale (a few milliseconds) throughout the epoch of 500 ms before the reward, with a precise relation to the low-γ frequency (mean frequency of peaks 33.6 Hz).

Figures 7A–7C show the correlation dynamics for one pair of units. To quantify the prevalence of these phenomena at the population level, we compared the CCH peaks calculated for the High-Power and Low-Power periods for all unit pairs (n = 1,031). We found that 18.8% (194) of all unit pairs had a significantly higher peak in the High-Power period. Calculating an averaged JPETH for all these 194 pairs (in the High-Power period) produced Figure 7E, which is quite similar to Figure 7B. Thus, a significant subset of neuronal pairs (18.8%) showed similar dynamic emergence of specific correlation patterns concurrently with the low-γ oscillations, which were generated behaviorally by the BMI conditioning task.

To further examine the relation of the low-γ power and the strength of pairwise synchrony, we plotted the depth of modulation of the CCHs of these pairs in five periods of increasing low-γ power (see Experimental Procedures). The plot (Figure 7H) shows that the pairwise synchrony strength increases gradually with increased low-γ power, demonstrating a proportional quantitative relation between low-γ power and spike synchrony.

Finally, in order to directly assess the relationship between phase-locked firing and the strength of pairwise neuronal correlations in the High-Power period, we calculated the phase-locking index (PLI) for each of the units to the low-γ oscillations on the same electrode and computed the average of the PLIs of the 2 units (Lachaux et al., 1999; see Supplemental Experimental Procedures). The PLI is a number from zero (0) to one (1) where 1 indicates perfect phase locking. Figure 7I depicts the depth of modulation of the CCH as a function of the averaged PLI for each pair. As expected, we found a strong positive correlation between these two variables (ρ = 0.81). This finding shows that when low-γ oscillations are sufficiently strong (as in our conditioning task), the phase locking of single-unit activity is a determining factor on the strength of neuronal correlations, and this relationship can be observed at the single-pair level.

Spatiotemporal Behavior of Low-γ Power across Cortex

This last section of the Results examines the spatiotemporal patterns of oscillations, phase-locked firing, and spike synchrony across the recording array.

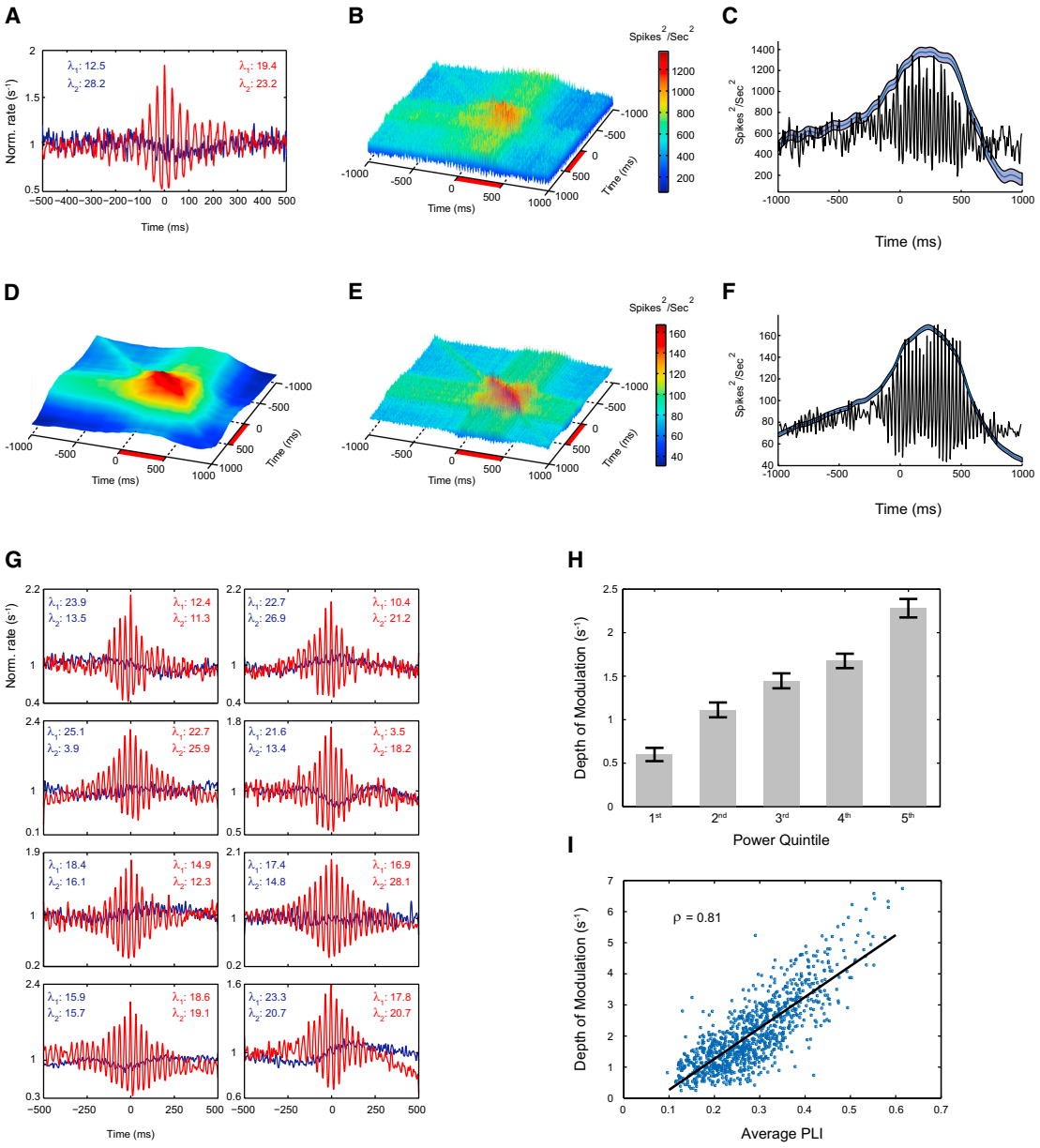

Figure 7. Pairwise Interactions of Phase-Locked Units

(A) CCH of 2 units in the High-Power (red) and Low-Power (blue) periods. Both units were phase locked to low-γ oscillations in the High-Power period (Figures 5B and 5E). Mean firing rates in hertz (Hz) are indicated in the plot.

(B) JPETH of the 2 units in (A), aligned to the first peak of the gamma cycle (phase = 0) around the beginning of the High-Power segment (time 0).

(C) Diagonal of the JPETH in (B) (black) and the mean ± SEM of the 30–43 Hz power of a single conditioned site (blue, arbitrary units, scaled to view).

(D) Joint amplitude of 30–43 Hz power of LFP for the 2 units' electrodes (a.u.).

(E) Mean JPETH of all pairs that showed significantly higher depth of modulation in their CCHs during the High-Power periods.

(F) Diagonal of the mean JPETH in (E) (black) and mean ± SEM of the 30–43 Hz power of a single conditioned site (blue, scaled to view).

(G) Examples of CCH for eight pairs, which showed significantly higher depth of modulation during the High-Power periods (red) as compared to the Low-Power period (blue). Mean firing rates in hertz (Hz) are indicated in the plots.

(H) Mean ± SEM of the depth of modulation of the CCHs for five groups of periods of increasing power of low γ, shown on the x axis. Data are from pairs that exhibited significantly increased depth of modulation in the High-Power period compared to the Low-Power period (see Experimental Procedures).

(I) Scatterplot of the depth of modulation of CCHs in the High-Power period as a function of the PLI average of the pair. The CC between these variables was 0.81. See also Figure S3.

The BMI algorithm utilized LFP low-γ power recorded from a subset of four adjacent electrodes. These selected electrodes were found to contain the highest low-γ power in preliminary recordings and served as the conditioned sites throughout all experiments.

First, to examine the spatial extent of the increase in low-γ power, we computed the instantaneous low-γ power for each electrode during the conditioning period using the Hilbert transform (see Experimental Procedures) and computed a peri-event time average (PETA) of instantaneous power aligned by reward delivery by averaging the power separately for each electrode. The results from one recording day are shown in Figures 8A and 8B. Sorting the electrodes by the mean power (Figure 8A) demonstrates the differences in temporal evolvement and maximum power across electrodes. To illustrate the spatiotemporal evolution of low-γ power across the array, we present nine still pictures of the instantaneous power on all electrodes, taken at different times along the trial (Figure 8B). The conditioned sites (Figure 8B, circled in white) showed an increase in low-γ power early in the trial with high power throughout. The power in the remainder of the array increased more gradually; on most electrodes, the maximal power was smaller, and some barely showed any increase. Similar structures were detected on all recording days for this monkey. In the other monkey, we also found a temporal and spatial structure that depended on the conditioned sites but with different orientations across the array (Figures 8G and S4).

These results demonstrate a spatiotemporal pattern that focuses around the location of the conditioned sites and decreases with the distance from it. To quantify this effect, we defined the "conditioning focus" as the geometric center of the conditioned sites. The correlation between the distance from the conditioning focus and the mean low-γ power in each electrode was −0.88 and −0.69 in monkeys Q and M, respectively.

Second, we examined the relation of the spatial structure of low-γ power to the phase-locked spike firing. Plotting the mean PLI for all units on each electrode as a function of its distance from the conditioning focus revealed a clear negative correlation between the two (Figure 8C, $\rho = -0.63$). This result indicates a spatial structure of phase-locked firing similar to the low-γ power structure: units fire with stronger phase locking the closer they are to the conditioning focus. To verify the similarity between the two spatial structures, we calculated the correlation between the average PLI and the mean low-γ power for all electrodes directly; the correlations were strongly positive for both monkeys ($\rho = 0.71$ and 0.7 for monkeys Q and M, respectively; Figure S4).

To gauge the spatial structure of neuronal synchrony, we estimated the "location" of each pair by the midpoint of the units' electrodes and used this estimate to calculate their distance from the conditioning focus. A smoothed surface plot (Figure 8D) shows, for all pairs, the relationship between this distance, the PLI average and the depth of modulation of the CCHs. The strength of neuronal correlations increased with proximity to the conditioning focus and strength of phase locking. These results further indicate that the conditioning scheme induced a topological structure of neuronal synchrony adhering closely to that of the low-γ oscillations.

Finally, we assessed whether focal generation of low-γ oscillations was accompanied by a topologically congruent increase in synchronization between LFPs in different sites. To do so, we computed the correlation coefficients (CCs) between LFPs of each site with the LFPs of the conditioned sites. These correlations were evaluated separately for the High-Power and the Low-Power periods (see Supplemental Experimental Procedures). The average CC differences between the two periods (Figure 8E, monkey M) exhibited a topological structure, similar to the spread of low-gamma power shown in Figure 8F ($\rho = 0.76$). The results for monkey Q were very similar (Figures 8G and 8H; $\rho = 0.81$ between the topological structures of oscillations and LFP synchronization). This result demonstrates that (1) LFP synchronization between the conditioned sites increased during the generation of low-γ oscillations, and (2) LFP synchronization between the nonconditioned and conditioned sites changed congruently with the increase in low-γ power across the array.

DISCUSSION

Oscillations in the low-gamma range have been found in many different brain areas and are associated with different functions such as attention, perception, and cognition (Herrmann et al., 2010). These oscillations are thought to play a pivotal role in brain computation (Fries, 2009) and neural synchrony both within (Salinas and Sejnowski, 2001) and between brain localities (Siegel et al., 2012). Previous reports have highlighted the relationship between low-gamma rhythms and precise synchronization of distributed neuronal responses, in particular in the visual cortex (Gray et al., 1989; Eckhorn et al., 1988; König et al., 1995).

Here, we showed (1) a tight linkage between the spatial patterns of low-gamma oscillations, spike synchronization and LFP correlations across cortical sites (Figure 8); (2) a quantitative relationship between the overall low-gamma power and the level of synchrony of neuronal ensembles (Figure 6); and (3) a strong relationship between the temporal dynamics of low-gamma power and those of precise time spike synchrony, which can wax and wane at the timescale of a few tens of milliseconds (Figure 7). These findings suggest a common mode of modulation of LFP low-gamma oscillations and spike synchrony. Moreover, the use of LFP low-gamma oscillations as the conditioned signal for the BMI effectively enabled volitional control of spatiotemporal patterns of precise time spike synchrony.

Significance of the Modulation of Low-Gamma Oscillations and Neuronal Synchrony

Different frequency bands of neural oscillations have been described in cortex, including theta (4–8 Hz), alpha or mu (8–12 Hz), beta (12–30 Hz), low-gamma (30–50 Hz), and higher frequencies (MacKay, 2005; Buzsáki and Draguhn, 2004). Previous studies have suggested a functional significance for each of these bands. Thus, any of these could in principle be used as a conditioning signal for BMI experiments. However, we chose to focus on the low-gamma band for two main reasons. First, as described above, low-gamma oscillations have been implicated in the synchronization of neural activity

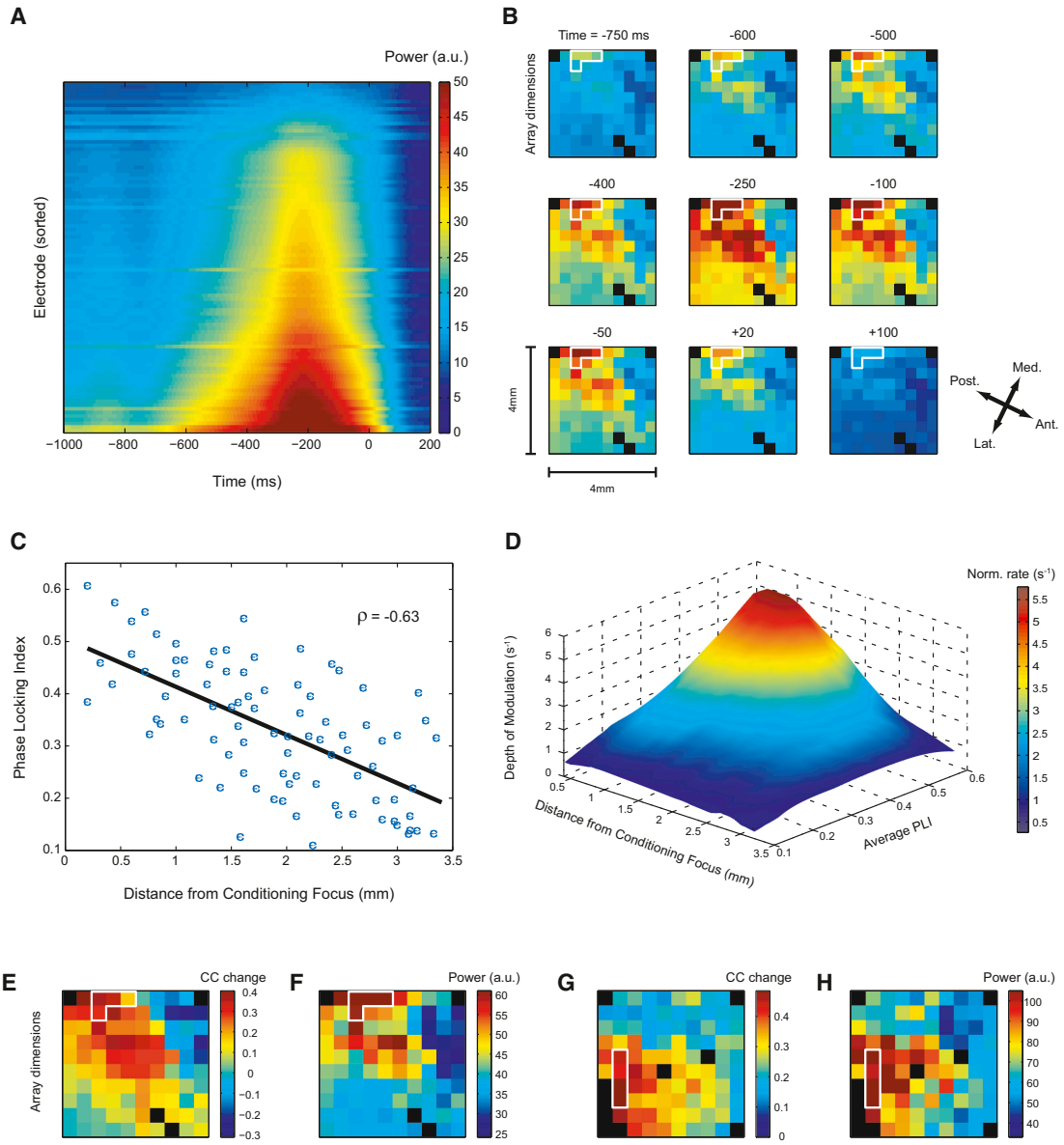

Figure 8. Spatiotemporal Dynamics of Low-γ Power during Conditioning

(A) Mean power of 30–43 Hz band for all electrodes aligned to reward delivery (time 0). Data are from a single session of monkey M. Electrodes were sorted according to their mean power.

(B) Snapshots of the mean power across the array at different times in the trial (−750 to +100 ms around the reward delivery). Each square is a single electrode of the array. The conditioned sites are circled in white. The four black squares (top corners and middle bottom) are nonrecording electrodes. Data are from the same session as (A). Post., posterior; Med., medial; Ant., anterior; Lat., lateral.

(C) Scatterplot of the average PLI of the units in each electrode as a function of the electrode's distance from the conditioning focus. CC is −0.63. Data are from the two monkeys.

(D) Smoothed surface plot showing the depth of modulation of the CCH of each pair as a function of the average PLI of the pair and the pair's estimated distance (see text) from the conditioning focus. Norm. rate, normalized rate. See also Figure S4.

(E) Changes in LFP synchronization of all sites with the conditioned sites are shown: color coded across the array is the average change in the CC of LFPs between each electrode and the four electrodes used for conditioning (circled in white; see Supplemental Experimental Procedures). The increase in LFP synchronization between the nonconditioned sites and the conditioned sites is tightly linked to the spread of 30–43 Hz power across the array during the generation of oscillations shown in (F). For the conditioned sites, the average was computed across the change of correlations of each electrode with the three other conditioned sites. Nonrecording electrodes are colored black. Data are an average over all successful conditioning sessions for monkey M.

(F) Average 30–43 Hz power in the Higher-Power period for all successful conditioning sessions of monkey M.

(G and H) Same as (E) and (F), for monkey Q.

Related to Figure S4.

with relation to behavior (Gray et al., 1989; Singer and Gray, 1995; Salinas and Sejnowski, 2001). Second, abnormal activity in the low-gamma band has been reported in a wide range of pathological brain states, including ADHD, epilepsy, schizophrenia, autism, Alzheimer's disease, and dyslexia (Başar and Güntekin, 2008; Herrmann and Demiralp, 2005; Lehongre et al., 2011). It has been hypothesized that dysfunctions in the mechanisms underlying gamma oscillations may account for some of the symptoms that accompany these conditions, largely by causing a breakdown in normal patterns of neural synchrony (Uhlhaas and Singer, 2012). Thus, our findings, which link the modulation of oscillations and precise time neuronal synchronization, suggest that accurate monitoring and modulation of low-gamma activity may become a beneficial clinical tool for a wide range of medical conditions.

Relationship to Previous Studies

The results of this study corroborate and extend previous investigations of spatiotemporal patterns of neuronal activity monitored at different resolutions.

Control of the low-gamma range in EEG was demonstrated long ago by biofeedback experiments in humans (Bird et al., 1978) and more recently by Keizer et al. (2010), indicating that conditioning can be used to alter brain activity in this frequency range. Additionally, EEG and fMRI studies have reported that biofeedback can alter cortical excitation (Sitaram et al., 2012; Ros et al., 2010). Naturally, these noninvasive studies could neither address the relations of EEG patterns to spike synchrony nor the detailed picture of the local cortical circuitry.

EEG biofeedback has been used to treat several disorders, particularly epilepsy (Angelakis et al., 2007) and ADD/ADHD (Loo and Barkley, 2005), by concentrating on subbands of beta (12–15 and 15–18 Hz) or lower frequencies. However, there is still debate concerning the efficacy of current clinical applications of EEG biofeedback protocols (Moriyama et al., 2012). Thus, further studies are still needed to translate the basic science knowledge into effective clinical applications.

In the motor cortex, oscillations in the high-beta and low-gamma ranges have been related to exploratory movements (Murthy and Fetz, 1992), movement preparation (Sanes and Donoghue, 1993; Donoghue et al., 1998), and attention (Saleh et al., 2010). In concert with these studies, our results suggest that oscillatory patterns of neuronal activity in motor cortex are present when this area is engaged in the control of behavior.

Alternative Interpretations

One alternative explanation of our results is that the increase in low-gamma power was a consequence of a specific type of movement by the monkeys. To investigate this possibility, several controls were implemented: video recordings of the monkeys' upper body, head, and upper portion of the legs were made in the conditioning period and did not show movements by the monkeys during the successful increase in low-gamma power, coinciding with earlier reports that showed a decrease of power at movement initiation in motor cortex (Sanes and Donoghue, 1993). Additionally, in several sessions, EMG was recorded from arm muscles. These EMG recordings did not show activity during successful task performance in the conditioning period (Figure S3).

Next, we tested whether the relations between low-gamma power increase and spike synchrony could arise from a general increase in firing rates of single units. This hypothesis was rejected in two ways:

(1) A comparison of the average firing rates during the Low- and High-Power periods showed that although many units either decreased or increased their firing rates, there was no significant overall trend. Overall firing rates decreased nonsignificantly (from the Low- to High-power periods) for the whole population and also for the subpopulation consisting only of units that were part of pairs sharing a significant increase in CCH peaks (Figure S3).

(2) All calculations of synchrony were adjusted to account for fluctuations of firing rates of the correlated units. It is therefore highly unlikely that the observed increase in synchrony was a result of changes in the firing rates of the single units.

Mechanisms Underlying Oscillatory Synchrony

The patterns of spike synchronization as revealed by the CCHs, JPETHs, and raster plots (Figures 6 and 7) are all clearly oscillatory and tightly linked to the spatiotemporal patterns of LFP low-gamma oscillations. We examined potential mechanisms that could explain these linked phenomena. One possibility is that the observed oscillations depend exclusively on intrinsic oscillatory properties of the sampled units. However, a previous study examining intracellular recordings of monkey M1 neurons found that a minority of their recorded neurons (termed "type III" in the study) exhibited such properties (Chen and Fetz, 2005). As suggested by the authors, this subpopulation could have a supporting role enhancing entrained oscillatory activity of the network.

It has been shown computationally that a strong oscillatory drive can evoke oscillations of synaptic currents and phase-locked firing of neurons (Brody and Hopfield, 2003). Oscillatory signals to motor cortex from sensory and posterior parietal cortices (Brovelli et al., 2004), as well as from subcortical structures (Steriade, 1995), have been previously identified. However, in cortex, there is converging evidence that network activity mediated by inhibitory interneurons is involved in generating low-gamma oscillations (Bartos et al., 2007; Buzsáki and Wang, 2012; Cardin et al., 2009). A study by Cardin et al. demonstrated that oscillatory stimulation of inhibitory neurons induced LFP oscillations in the low-gamma range, whereas the same stimulation to the pyramidal cells failed to do so (Cardin et al., 2009). Note that most of the phase-locked cells we recorded are putatively pyramidal cells because our recordings are biased toward the sampling of large neurons in the deep layers of motor cortex. Accordingly, external excitatory drive to the recorded cells is less likely to be sufficient to evoke the observed LFP oscillations and oscillatory spike synchrony. Furthermore, there is support for the hypothesis that inhibitory feedback mediates oscillations in primary motor cortex (Jackson et al., 2002).

Additionally, it has been suggested that impaired function of these inhibitory populations could be related to cognitive deficits (Lewis et al., 2012).

The data and theory presented above suggest that inhibitory neurons play a role in the generation of gamma oscillations and the concurrent spike synchrony observed in our study. However, this is a hypothesis that remains to be tested directly. A related open issue is the mechanism underlying the spatial spread of the synchrony, which could depend on the spatial structure of inhibitory connectivity across the network. These fundamental questions can be addressed in future studies; in particular, using novel methods that allow for selective activation or suppression of inhibitory and excitatory neurons (Atallah et al., 2012). Such localized manipulations could elucidate the impact of inhibitory neurons on the generation and spatial spread of gamma oscillations and spike synchronization.

Conclusions

We presented a method that allows focal modulation of low-gamma oscillations, effectively enabling focal, volitional control of precise temporal synchrony. Our findings indicate that the brain has the capacity to rapidly modulate the level of synchronization of neuronal groups in specific temporal and spatial domains and in a specific behavioral context. These results are especially significant because dynamic modulations of neuronal interactions are thought to underlie behavioral processes and to be an important feature of cortical computation (Abeles, 1991; Vaadia et al., 1995; Riehle et al., 1997; Kayser et al., 2009). The ability to use operant conditioning in a BMI setting to control synchrony at the level of single units paves the way for use of high-resolution BMIs for future clinical applications and as a powerful tool for understanding processes of neural computation.

EXPERIMENTAL PROCEDURES

Animals and Surgical Procedure

Two monkeys (*Macaca fascicularis*) were chronically implanted with a microelectrode array (Blackrock Microsystems) in the arm region of M1 contralateral to the performing arm, under anesthesia and aseptic conditions. Animal care and surgical procedures complied with the National Institutes of Health Guide for the Care and Use of Laboratory Animals and with guidelines defined by the Institutional Committee for Animal Care and Use at the Hebrew University.

Behavioral Task

A single recording session was composed of four blocks. The first and last blocks (movement blocks) consisted of a center-out task, with grip-and-reach movements to eight targets located at the corners of a three-dimensional cube. The monkeys used a robotic arm (Phantom Premium 1.5 High Force; SensAble Devices) and a custom-made gripping handle to control the movements. The monkeys could not see their arms. Instead, images of targets and cursor were projected to the arm workspace. The cursor represented the hand location and grip force. Targets were defined as spheres of 8 mm radii, and the distance between the center of the origin and the center of each target was 4.85 cm. In the conditioning block (third block of the session), the cursor and target were displayed in similar sizes and distances as in the movement blocks, but the monkeys' arms were restrained, and the cursor position was determined by the mean power of the 30–43 Hz band (low γ) of LFP recorded from a selected group of electrodes. The details of the conditioning algorithm are described below.

Prior to the conditioning block, we employed a control block termed "pseudoconditioning" (Figure 1A, second block of the session). In this block, conditions were the same as in the conditioning block except that the cursor position was determined randomly each 100 ms, hence resulting in random delivery of reward. Additionally, four small red spheres located in the corners of the workspace were lit throughout the duration of this block to indicate the "pseudoconditioning" state.

Electrophysiology

The recording array was composed of 100 electrodes (Blackrock Microsystems), of which 96 were functional, arranged in a 10×10 matrix with 400 μm interelectrode distance. LFP signals were collected at a 1 KHz sampling rate and filtered using a 0.3–250 Hz band-pass filter. Spikes were extracted from the raw signal, sampled at 30 KHz, and manually sorted using the histogram peak count algorithm. LFP and spikes were collected using the Cerebus data acquisition system (Blackrock Microsystems). In monkey Q, six of the electrodes were damaged during surgery and were not analyzed further. A total of 44 recording sessions were analyzed (26 from monkey M, 18 from monkey Q). Of these, 16 sessions were considered successful conditioning sessions (see below) and were analyzed in further detail. In several sessions, EMG signals were obtained using double-differential surface electrodes (Motion Lab Systems). EMG signals were filtered (0.01–3 KHz), sampled at 10 KHz, and stored. EMG signals were then rectified and smoothed with a Gaussian kernel (SD = 25 ms).

Conditioning Algorithm

For each monkey, four adjacent electrodes were chosen for conditioning. During the conditioning block, we computed the LFP power in a window of the last 500 ms. The window was recalculated every 100 ms. The mean 30–43 Hz power was calculated for each channel using the average discrete Fourier transform (DFT) coefficients (in absolute power) in the specified frequency range. The cutoff at 43 Hz was chosen for technical reasons to avoid artifacts due to the power supply frequency (50 Hz). The mean power obtained from the four selected electrodes was further averaged to obtain the overall mean. The cursor was positioned on the line between the origin and the target, with a linear correspondence (gain) to the overall mean power, truncated by a minimum value (below which the cursor was placed in the origin) and a maximum value above which the cursor was placed in the target, a reward was delivered, and the trial ended. The linear gain between the overall mean power and cursor position was adjusted manually during the block to provide a relatively constant rate of reward, thus encouraging the monkeys to continuously improve their performance.

To avoid effects of artifactual broadband increases in the power spectrum, we also applied a rejection criterion for windows where the mean high-frequency power (120–180 Hz) increased significantly. In these windows, the cursor was placed in the origin.

Data Analysis

All postprocessing was performed in MATLAB (MathWorks). The power spectrum was calculated using the DFT coefficients in segments of 0.5 s. The mean 30–43 Hz power for a given block in a single session was the average power of all 0.5 s segments in the block. A successful conditioning session was such that the ratio between the mean power in the conditioning and the first movement block was at least 1.25.

To compute the instantaneous power, the 30–43 Hz band was first extracted using a zero-phase shift, bidirectional Kaiser filter with a stop-band attenuation of 80 dB and pass-band ripple of 0.005 dB. The instantaneous power was then calculated via the magnitude of the analytic signal obtained using the Hilbert transform (Le Van Quyen et al., 2001). The phase of the Hilbert transform was used to calculate the instantaneous phase at spike times.

High- and Low-Power Periods

We first divided the conditioning block into nonoverlapping segments of 0.5 s. We calculated the mean 30–43 Hz power for each segment using the DFT. All segments were then sorted according to the power. The 500 segments with the lowest power were labeled the Low-Power period, and the 500 segments

with the highest power were labeled the High-Power period. Segments from the two periods constantly alternated with the monkey's instantaneous performance.

To obtain five periods with increasing power (Figures 6C and 7H), we followed the same procedure (the highest- and lowest-power periods were the same) and divided the sorted conditioning block into five equal parts. The central 500 segments from the middle three parts made up the middle three power periods.

Alignment of Neural Data

To temporally align trials with respect to the low-γ oscillation cycle, we first chose an alignment point in the trial, either 500 ms before reward delivery (Figures 4, 5, and 6) or the beginning of a 500 ms segment of the High-Power period (Figure 7). We then calculated the mean phase of the 30–43 Hz LFP band in the 500 ms following the alignment point using the DFT. Finally, we shifted all neural data (spikes and LFP together) in that trial, so that this phase would be zero (0) (peak of the low-γ oscillations). The resulting shift was bounded by ±16 ms and allowed proper averaging of the low-γ cycle.

Preferred Phases and Time Interval of Preferred Phase Firing

The preferred phase for each unit was computed as the (angular) average spike time phase. The significance of the preferred phase was assessed by a Raleigh test with a significance p value threshold of 0.0001 with a Bonferroni correction.

We next examined which fractions of units preferentially fired within a given time interval. To do so, we chose units with a significant preferred phase in the High-Power period (Figure 5F, right, black histogram). Centering on the median of this distribution, we chose symmetric sections, which included increasing fractions of units (from 50% to 95% of the units; x axis of Figure 5G). For each fraction of units (section size), we computed the maximal interval within which all units fired preferentially. This was done by computing the time interval corresponding to the section size assuming a cycle frequency of 35 Hz.

Probability of Coordinated Firing

After obtaining five periods of increasing power (see above) in a conditioning block of a successful session, the probability of coordinated firing was estimated as follows: each of the five periods was divided into 500 segments of 0.5 s, and for each segment we counted, in all 5 ms bins, the number of units that fired at least one spike in the bin. This count was normalized by the total number of bins and total number of spikes of all units in the segment. From the sample of normalized counts, we obtained the mean and SEM values across segments and days. To account for the differing number of recorded units across days, we randomly chose 11 units on which to perform this procedure each day (the minimum number of units recorded in a successful session), repeated the procedure 100 times for each day with a different random selection of units, and averaged the results.

Cross-Correlogram Histogram and JPETH

For the CCH calculation, the two neuronal spike trains were binned in 1 ms bins, and one of them was chosen randomly as the trigger unit. For each spike in the trigger unit, a count vector was updated in place t when there was a spike in the second unit t time bins away, $t \in \{-500, \ldots, 500\}$. The count vector was then normalized by the total number of triggered spikes to allow comparison of CCHs in different conditions and different firing rates. The CCH was smoothed with a zero-phase Gaussian filter with 2 ms SD. The depth of modulation of the CCH was estimated as the maximum difference between CCH values in the ±20 ms range, for pairs of units that had at least 100 triggered spikes. For the depth of modulation calculations, the CCH was computed with a maximum lag of 150 ms. The significance of the difference between CCH depths of modulation in the High- and Low-Power periods was estimated by recalculating the CCHs using bootstrap techniques with 10,000 iterations and a p value of 0.001 with a Bonferroni correction.

The JPETH (Aertsen et al., 1989) was calculated by binning the two spike trains in 10 ms bins and choosing one of them randomly as the trigger unit. For each bin in time t_1 where the trigger unit fired at least one spike, the JPETH matrix was updated at (t_1, t_2) if the second unit fired at least one spike in bin t_2 in the same trial. To calculate the mean frequency of peaks in the main diagonal, the procedure was repeated with a 5 ms bin.

Comparison of Firing Rates in the High- and Low-Power Periods

To compare firing rates in the two periods, for each unit, we computed the average firing rates in each of the 500 segments of 0.5 s composing each period. Significance was estimated using a two-tailed t test with a significance p value threshold of 0.0001 with a Bonferroni correction. Firing rate differences of all units in the two periods were also compared using a two-tailed t test. The same procedure was also applied separately for the units that were part of a pair exhibiting a significant increase in depth of modulation in the High-Power period.

SUPPLEMENTAL INFORMATION

Supplemental Information includes four figures and Supplemental Experimental Procedures and can be found with this article online at http://dx.doi.org/10.1016/j.neuron.2012.11.015.

ACKNOWLEDGMENTS

We thank I. Novick for help with the EMG recordings; E. Ahissar, I. Novick, and M. London for their helpful comments; A. Raz for help with the surgeries; and S. Freeman and A. Shapochnikov for technical assistance. This work was supported in part by the Binational Science Foundation (BSF), the Israel Science Foundation, special contributions from the Rosetrees Trust, the Gatsby Charitable Foundation, and the Ida Baruch Fund. B.E. was partly supported by the Felix M. Katar fund. This work is dedicated to the memory of Dr. Dmitry Davidov. The authors are currently preparing a patent application that is partly based on the results of this study.

Accepted: November 13, 2012
Published: January 23, 2013

REFERENCES

Abeles, M. (1991). Corticonics: Neural Circuits of the Cerebral Cortex (New York: Cambridge University Press).

Aertsen, A.M., Gerstein, G.L., Habib, M.K., and Palm, G. (1989). Dynamics of neuronal firing correlation: modulation of "effective connectivity". J. Neurophysiol. *61*, 900–917.

Angelakis, E., Stathopoulou, S., Frymiare, J.L., Green, D.L., Lubar, J.F., and Kounios, J. (2007). EEG neurofeedback: a brief overview and an example of peak alpha frequency training for cognitive enhancement in the elderly. Clin. Neuropsychol. *21*, 110–129.

Apostol, G., and Creutzfeldt, O.D. (1974). Crosscorrelation between the activity of septal units and hippocampal EEG during arousal. Brain Res. *67*, 65–75.

Atallah, B.V., Bruns, W., Carandini, M., and Scanziani, M. (2012). Parvalbumin-expressing interneurons linearly transform cortical responses to visual stimuli. Neuron *73*, 159–170.

Averbeck, B.B., Latham, P.E., and Pouget, A. (2006). Neural correlations, population coding and computation. Nat. Rev. Neurosci. *7*, 358–366.

Bartos, M., Vida, I., and Jonas, P. (2007). Synaptic mechanisms of synchronized gamma oscillations in inhibitory interneuron networks. Nat. Rev. Neurosci. *8*, 45–56.

Başar, E., and Güntekin, B. (2008). A review of brain oscillations in cognitive disorders and the role of neurotransmitters. Brain Res. *1235*, 172–193.

Bird, B.L., Newton, F.A., Sheer, D.E., and Ford, M. (1978). Biofeedback training of 40-Hz EEG in humans. Biofeedback Self Regul. *3*, 1–11.

Brody, C.D., and Hopfield, J.J. (2003). Simple networks for spike-timing-based computation, with application to olfactory processing. Neuron *37*, 843–852.

Brovelli, A., Ding, M., Ledberg, A., Chen, Y., Nakamura, R., and Bressler, S.L. (2004). Beta oscillations in a large-scale sensorimotor cortical network:

directional influences revealed by Granger causality. Proc. Natl. Acad. Sci. USA *101*, 9849–9854.

Buzsáki, G., and Draguhn, A. (2004). Neuronal oscillations in cortical networks. Science *304*, 1926–1929.

Buzsáki, G., and Wang, X.J. (2012). Mechanisms of gamma oscillations. Annu. Rev. Neurosci. *35*, 203–225.

Cardin, J.A., Carlén, M., Meletis, K., Knoblich, U., Zhang, F., Deisseroth, K., Tsai, L.H., and Moore, C.I. (2009). Driving fast-spiking cells induces gamma rhythm and controls sensory responses. Nature *459*, 663–667.

Chen, D., and Fetz, E.E. (2005). Characteristic membrane potential trajectories in primate sensorimotor cortex neurons recorded in vivo. J. Neurophysiol. *94*, 2713–2725.

Denker, M., Roux, S., Lindén, H., Diesmann, M., Riehle, A., and Grün, S. (2011). The local field potential reflects surplus spike synchrony. Cereb. Cortex *21*, 2681–2695.

Donoghue, J.P., Sanes, J.N., Hatsopoulos, N.G., and Gaál, G. (1998). Neural discharge and local field potential oscillations in primate motor cortex during voluntary movements. J. Neurophysiol. *79*, 159–173.

Eckhorn, R., Bauer, R., Jordan, W., Brosch, M., Kruse, W., Munk, M., and Reitboeck, H.J. (1988). Coherent oscillations: a mechanism of feature linking in the visual cortex? Multiple electrode and correlation analyses in the cat. Biol. Cybern. *60*, 121–130.

Fetz, E.E. (1969). Operant conditioning of cortical unit activity. Science *163*, 955–958.

Fries, P. (2009). Neuronal gamma-band synchronization as a fundamental process in cortical computation. Annu. Rev. Neurosci. *32*, 209–224.

Gray, C.M., and Singer, W. (1989). Stimulus-specific neuronal oscillations in orientation columns of cat visual cortex. Proc. Natl. Acad. Sci. USA *86*, 1698–1702.

Gray, C.M., König, P., Engel, A.K., and Singer, W. (1989). Oscillatory responses in cat visual cortex exhibit inter-columnar synchronization which reflects global stimulus properties. Nature *338*, 334–337.

Herrmann, C.S., and Demiralp, T. (2005). Human EEG gamma oscillations in neuropsychiatric disorders. Clin. Neurophysiol. *116*, 2719–2733.

Herrmann, C.S., Fründ, I., and Lenz, D. (2010). Human gamma-band activity: a review on cognitive and behavioral correlates and network models. Neurosci. Biobehav. Rev. *34*, 981–992.

Jackson, A., Spinks, R.L., Freeman, T.C., Wolpert, D.M., and Lemon, R.N. (2002). Rhythm generation in monkey motor cortex explored using pyramidal tract stimulation. J. Physiol. *541*, 685–699.

Kayser, C., Montemurro, M.A., Logothetis, N.K., and Panzeri, S. (2009). Spike-phase coding boosts and stabilizes information carried by spatial and temporal spike patterns. Neuron *61*, 597–608.

Keizer, A.W., Verschoor, M., Verment, R.S., and Hommel, B. (2010). The effect of gamma enhancing neurofeedback on the control of feature bindings and intelligence measures. Int. J. Psychophysiol. *75*, 25–32.

Koenig, T., Prichep, L., Dierks, T., Hubl, D., Wahlund, L.O., John, E.R., and Jelic, V. (2005). Decreased EEG synchronization in Alzheimer's disease and mild cognitive impairment. Neurobiol. Aging *26*, 165–171.

König, P., Engel, A.K., and Singer, W. (1995). Relation between oscillatory activity and long-range synchronization in cat visual cortex. Proc. Natl. Acad. Sci. USA *92*, 290–294.

Lachaux, J.P., Rodriguez, E., Martinerie, J., and Varela, F.J. (1999). Measuring phase synchrony in brain signals. Hum. Brain Mapp. *8*, 194–208.

Lehongre, K., Ramus, F., Villiermet, N., Schwartz, D., and Giraud, A.L. (2011). Altered low-γ sampling in auditory cortex accounts for the three main facets of dyslexia. Neuron *72*, 1080–1090.

Le Van Quyen, M., Foucher, J., Lachaux, J., Rodriguez, E., Lutz, A., Martinerie, J., and Varela, F.J. (2001). Comparison of Hilbert transform and wavelet methods for the analysis of neuronal synchrony. J. Neurosci. Methods *111*, 83–98.

Lewis, D.A., Curley, A.A., Glausier, J.R., and Volk, D.W. (2012). Cortical parvalbumin interneurons and cognitive dysfunction in schizophrenia. Trends Neurosci. *35*, 57–67.

Loo, S.K., and Barkley, R.A. (2005). Clinical utility of EEG in attention deficit hyperactivity disorder. Appl. Neuropsychol. *12*, 64–76.

MacKay, W.A. (2005). Wheels of motion: oscillatory potentials in the motor cortex. In Motor Cortex in Voluntary Movements: A Distributed System for Distributed Functions, A. Riehle and E. Vaadia, eds. (Boca Raton, FL: CRC Press), pp. 210–242.

Moriyama, T.S., Polanczyk, G., Caye, A., Banaschewski, T., Brandeis, D., and Rohde, L.A. (2012). Evidence-based information on the clinical use of neurofeedback for ADHD. Neurotherapeutics *9*, 588–598.

Murthy, V.N., and Fetz, E.E. (1992). Coherent 25- to 35-Hz oscillations in the sensorimotor cortex of awake behaving monkeys. Proc. Natl. Acad. Sci. USA *89*, 5670–5674.

Murthy, V.N., and Fetz, E.E. (1996). Synchronization of neurons during local field potential oscillations in sensorimotor cortex of awake monkeys. J. Neurophysiol. *76*, 3968–3982.

Nunez, P.L., and Srinivasan, R. (2010). Scale and frequency chauvinism in brain dynamics: too much emphasis on γ band oscillations. Brain Struct. Funct. *215*, 67–71.

Palanca, B.J.A., and DeAngelis, G.C. (2005). Does neuronal synchrony underlie visual feature grouping? Neuron *46*, 333–346.

Riehle, A., Grün, S., Diesmann, M., and Aertsen, A. (1997). Spike synchronization and rate modulation differentially involved in motor cortical function. Science *278*, 1950–1953.

Ros, T., Munneke, M.A., Ruge, D., Gruzelier, J.H., and Rothwell, J.C. (2010). Endogenous control of waking brain rhythms induces neuroplasticity in humans. Eur. J. Neurosci. *31*, 770–778.

Saleh, M., Reimer, J., Penn, R., Ojakangas, C.L., and Hatsopoulos, N.G. (2010). Fast and slow oscillations in human primary motor cortex predict oncoming behaviorally relevant cues. Neuron *65*, 461–471.

Salinas, E., and Sejnowski, T.J. (2001). Correlated neuronal activity and the flow of neural information. Nat. Rev. Neurosci. *2*, 539–550.

Sanes, J.N., and Donoghue, J.P. (1993). Oscillations in local field potentials of the primate motor cortex during voluntary movement. Proc. Natl. Acad. Sci. USA *90*, 4470–4474.

Shadlen, M.N., and Movshon, J.A. (1999). Synchrony unbound: a critical evaluation of the temporal binding hypothesis. Neuron *24*, 67–77, 111–125.

Shmiel, T., Drori, R., Shmiel, O., Ben-Shaul, Y., Nadasdy, Z., Shemesh, M., Teicher, M., and Abeles, M. (2005). Neurons of the cerebral cortex exhibit precise interspike timing in correspondence to behavior. Proc. Natl. Acad. Sci. USA *102*, 18655–18657.

Siegel, M., Donner, T.H., and Engel, A.K. (2012). Spectral fingerprints of large-scale neuronal interactions. Nat. Rev. Neurosci. *13*, 121–134.

Singer, W. (1999). Neuronal synchrony: a versatile code for the definition of relations? Neuron *24*, 49–65, 111–125.

Singer, W., and Gray, C.M. (1995). Visual feature integration and the temporal correlation hypothesis. Annu. Rev. Neurosci. *18*, 555–586.

Sitaram, R., Veit, R., Stevens, B., Caria, A., Gerloff, C., Birbaumer, N., and Hummel, F. (2012). Acquired control of ventral premotor cortex activity by feedback training: an exploratory real-time FMRI and TMS study. Neurorehabil. Neural Repair *26*, 256–265.

Steriade, M. (1995). Two channels in the cerebellothalamocortical system. J. Comp. Neurol. *354*, 57–70.

Tiesinga, P., Fellous, J.M., and Sejnowski, T.J. (2008). Regulation of spike timing in visual cortical circuits. Nat. Rev. Neurosci. *9*, 97–107.

Uhlhaas, P.J., and Singer, W. (2006). Neural synchrony in brain disorders: relevance for cognitive dysfunctions and pathophysiology. Neuron *52*, 155–168.

Uhlhaas, P.J., and Singer, W. (2010). Abnormal neural oscillations and synchrony in schizophrenia. Nat. Rev. Neurosci. *11*, 100–113.

Uhlhaas, P.J., and Singer, W. (2012). Neuronal dynamics and neuropsychiatric disorders: toward a translational paradigm for dysfunctional large-scale networks. Neuron *75*, 963–980.

Vaadia, E., Haalman, I., Abeles, M., Bergman, H., Prut, Y., Slovin, H., and Aertsen, A. (1995). Dynamics of neuronal interactions in monkey cortex in relation to behavioural events. Nature *373*, 515–518.

Wilson, T.W., Rojas, D.C., Reite, M.L., Teale, P.D., and Rogers, S.J. (2007). Children and adolescents with autism exhibit reduced MEG steady-state gamma responses. Biol. Psychiatry *62*, 192–197.

Yuval-Greenberg, S., Tomer, O., Keren, A.S., Nelken, I., and Deouell, L.Y. (2008). Transient induced gamma-band response in EEG as a manifestation of miniature saccades. Neuron *58*, 429–441.